Monthly Notices of the ROYAL ASTRONOMICAL SOCIETY

MNRAS **532,** 613–621 (2024) https://doi.org/10.1093/mnras/stae1441
Advance Access publication 2024 June 17

The properties of AGN in dwarf galaxies identified via SED fitting

B. Bichang'a [1]★ S. Kaviraj [1] I. Lazar [1] R. A. Jackson,[2] S. Das [1] D. J. B. Smith,[1] A. E. Watkins[1] and G. Martin [3]

[1]*Centre for Astrophysics Research, University of Hertfordshire, Hatfield AL10 9AB, UK*
[2]*Department of Physics and Astronomy, University of Victoria, Victoria, BC V8P 5C2, Canada*
[3]*School of Physics and Astronomy, University of Nottingham, University Park, Nottingham NG7 2RD, UK*

Accepted 2024 June 3. Received 2024 May 28; in original form 2024 May 8

ABSTRACT

Given their dominance of the galaxy number density, dwarf galaxies are central to our understanding of galaxy formation. While the incidence of active galactic nuclei (AGN) and their impact on galaxy evolution have been extensively studied in massive galaxies, much less is known about the role of AGN in the evolution of dwarfs. We search for radiatively efficient AGN in the nearby ($0.1 < z < 0.3$) dwarf (10^8 M$_\odot$ $< M_\star <$ 10^{10} M$_\odot$) population, using spectral energy distribution fitting (via PROSPECTOR) applied to deep ultraviolet to mid-infrared photometry of 508 dwarf galaxies. Around a third (32 ± 2 per cent) of our dwarfs show signs of AGN activity. We compare the properties of our dwarf AGN to control samples, constructed from non-AGN, which have the same distributions of redshift and stellar mass as their AGN counterparts. Kolmogorov–Smirnov tests between the AGN and control distributions indicate that the AGN do not show differences in their distances to nodes, filaments, and nearby massive galaxies from their control counterparts. This indicates that AGN triggering in the dwarf regime is not strongly correlated with local environment. The fraction of AGN hosts with early-type morphology and those that are interacting are also indistinguishable from the controls within the uncertainties, suggesting that interactions do not play a significant role in inducing AGN activity in our sample. Finally, the star formation activity in dwarf AGN is only slightly lower than that in their control counterparts, suggesting that the presence of radiatively efficient AGN does not lead to significant, prompt quenching of star formation in these systems.

Key words: galaxies: active – galaxies: dwarf – galaxies: evolution – galaxies: formation – galaxies: interactions.

1 INTRODUCTION

The steep rise in the galaxy stellar mass function in the dwarf ($M_\star$ $< 10^{10}$ M$_\odot$) regime (e.g. Wright et al. 2017; Martin et al. 2019; Driver et al. 2022) indicates that dwarf galaxies dominate the galaxy number density at all redshifts and in all environments. This makes them vital, both for our empirical understanding of galaxy evolution and for constraining theoretical models. Our current picture of how galaxies evolve is largely based on massive galaxies, since these objects are bright enough to be detectable, across a large range in redshift, in past wide-area surveys (e.g. Jackson et al. 2021).

The properties of dwarf galaxies have been studied in detail in our local neighbourhood, out to distances of ∼50 Mpc (e.g. Mateo 1998; Tolstoy, Hill & Tosi 2009). However, typical dwarfs become undetectable at cosmological distances, in past surveys like the Sloan Digital Sky Survey (SDSS; York et al. 2000; Alam et al. 2015), which offer large footprints but are relatively shallow (e.g. Jackson et al. 2021; Lazar et al. 2024). In the specific case of the SDSS, it is worth noting that, while the limiting magnitude of its standard depth imaging is $r \sim 22.7$, many scientific analyses, including past dwarf studies using the SDSS, use the spectroscopic main galaxy sample (MGS). The MGS, however, has a much shallower magnitude limit of $r \sim 17.77$ (Strauss et al. 2002). The dwarfs that exist in data sets like the SDSS MGS tend to have high star formation rates (SFRs), which boost their luminosities above the detection thresholds of shallow surveys but also bias them towards systems that are blue, star-forming, and potentially dominated by late-type morphologies (e.g. Lazar et al. 2024).

The advent of new surveys that are both deep and wide, like the recent Hyper Suprime-Cam Subaru Strategic Program (HSC-SSP; Aihara et al. 2018) and, in the near future, Rubin Observatory's Legacy Survey of Space and Time (LSST; Ivezić et al. 2019), offers optical photometry with unprecedented depth over large areas of the sky. Such data sets can be used to identify dwarfs down to $M_\star \sim 10^8$ M$_\odot$ out to at least $z \sim 0.3$ (Jackson et al. 2021). In conjunction with similarly deep surveys at ancillary wavelengths, such data sets are likely to transform our understanding of the dwarf regime outside the very local Universe. It is worth noting that the shallow potential wells of dwarf galaxies are more sensitive to key processes that affect galaxy evolution [e.g. ram pressure stripping, tidal interactions, and baryonic feedback from stars and active galactic nuclei (AGN)] than massive galaxies (Martin et al. 2019). Statistical studies of dwarfs outside the local neighbourhood are therefore likely to lead to significant gains in our understanding of the physics of galaxy evolution.

★ E-mail: b.bichanga@herts.ac.uk

A prominent topic in the recent literature is the presence of black holes (BHs) and the role of AGN in galaxy evolution. The massive-galaxy regime is well studied in this context, with both observations and theory suggesting that not only do all massive systems likely host BHs (Richstone et al. 1998), but star formation activity, and therefore the growth of the host galaxy, is heavily influenced by AGN feedback (e.g. Fabian 2012; Beckmann et al. 2017; Kaviraj et al. 2017; Davies et al. 2024). However, less is currently known about the presence of BHs in dwarfs and their potential role in driving galaxy evolution in this regime (e.g. Silk 2017; Volonteri, Habouzit & Colpi 2021). While there is accumulating observational evidence of AGN in dwarf galaxies (e.g. Greene & Ho 2007; Reines, Greene & Geha 2013; Marleau et al. 2017; Nyland et al. 2017; Mezcua et al. 2018; Satyapal, Abel & Secrest 2018; Kaviraj, Martin & Silk 2019; Mezcua, Suh & Civano 2019; Baldassare, Geha & Greene 2020; Davis et al. 2022), questions persist regarding their frequency, the processes that might trigger the BHs, correlations with local environment, and whether feedback from the AGN can have a similar impact in dwarfs as it does in the massive-galaxy regime. It is worth noting that, in the dwarf regime, BHs tend not to grow in current cosmological simulations. This is either because the BHs wander for significant fractions of their lifetimes in regions of low gas density, away from the barycentres of the galaxies, or because supernova feedback displaces material around the BH and prevents it from feeding (e.g. Dubois et al. 2021). However, it remains unclear whether this behaviour truly mimics that of real dwarf galaxies or may be a result of the characteristics of such simulations (e.g. their relatively low mass and spatial resolutions). Empirical constraints on the incidence of AGN in dwarfs and the properties of their host galaxies are therefore valuable.

While AGN emission contributes to all parts of the spectral energy distribution (SED), the samples of AGN recovered from probing specific wavelength ranges differ, with unique challenges experienced in the different methods that are employed. For example, AGN selection based on X-ray luminosity (e.g. Latimer et al. 2019) may not be ideal for identifying AGN in the dwarf regime, due to the long exposure times required to detect low-luminosity AGN (e.g. Reines et al. 2020). AGN selection in dwarfs via optical variability (e.g. Baldassare et al. 2020; Martínez-Palomera et al. 2020) ideally requires optical surveys that are both deep and wide, to ensure that the dwarfs being studied do not suffer from the biases in shallow surveys described above. Employing emission-line diagnostics (e.g. Baldwin, Phillips & Terlevich 1981; Kewley et al. 2001; Cid Fernandes et al. 2010, 2011) to detect AGN in dwarfs in shallow surveys may similarly miss some AGN. This is because, if dwarfs in such surveys are biased towards star-forming systems, then the impact of the AGN on the emission lines may be dominated by the star formation activity.

Several studies in the literature have used radio excess to detect AGN (e.g. Gürkan et al. 2018; Lofthouse et al. 2018, Drake et al., in preparation). However, an implementation of this technique on data from the LOFAR Two-metre Sky Survey (Shimwell et al. 2019) indicates that, given the lower radio luminosities of dwarf AGN, only young radio AGN are likely to be found in dwarf galaxies (e.g. Davis et al. 2022), even in the deepest high-resolution radio surveys that are currently available.

In this context, SED fitting (e.g. Leja et al. 2018), using deep multiwavelength broad-band photometry, is a useful avenue for identifying AGN in dwarf galaxies (e.g. Delvecchio et al. 2014, 2017; Thorne et al. 2022; Best et al. 2023; Das et al. 2024). Using the full SED simultaneously leverages the impact of the AGN over a range of wavelengths. Furthermore, since high signal-to-noise ratio observations of fainter objects like dwarfs are easier to achieve via broad-band photometry, more complete samples of dwarfs can be probed for the presence of AGN, at least in the nearby Universe. The purpose of this paper is to use deep broad-band multiwavelength photometry to search for dwarfs that exhibit signs of AGN at low redshift ($z < 0.3$), probe the role of interactions and environment in AGN triggering, and study whether there is evidence for significant prompt quenching of star formation in these systems.

This paper is organized as follows. In Section 2, we describe the broad-band photometric data that are used in the SED fitting, the calculation of environmental parameters, the selection of our sample of dwarf galaxies, and the morphological classification of these systems using *Hubble Space Telescope* (*HST*) images. In Section 3, we describe the calculation of physical parameters using the SED-fitting code PROSPECTOR (Johnson et al. 2019, 2021; Leja et al. 2019). In Section 4, we use the outputs of our SED fitting to explore the incidence of AGN in our dwarf galaxies, study the role of interactions and local environment in AGN triggering, and compare the star formation activity in AGN and non-AGN to explore the possibility of AGN-driven quenching. We summarize our findings in Section 5.

2 DATA

2.1 The COSMOS2020 catalogue

We employ photometric data from the Classic version of the COSMOS2020 catalogue (Weaver et al. 2022), which provides deep multiwavelength ultraviolet (UV) to mid-infrared (MIR) photometric data in the COSMOS field. Notable improvements in this catalogue compared to its predecessor, the COSMOS2015 catalogue (Laigle et al. 2016), are the incorporation of ultradeep optical (*griz*) data from the HSC-SSP (Aihara et al. 2018) for object detection, improved *Spitzer*/IRAC data processing using IRACLEAN, and improved astrometric precision from aligning the imaging data with the *Gaia* DR1 (Gaia Collaboration 2016).The optical HSC photometry has a point source depth of ∼28 mag, significantly deeper than past surveys such as the SDSS (in which the optical images are ∼5 mag shallower than those from the HSC in COSMOS). We refer readers to Weaver et al. (2022) for further details of the processing of the photometric data.

We use total magnitudes from 15 broad-band filters that span the full UV to MIR wavelength range provided by the catalogue from the following surveys: *FUV* and *NUV* data from *GALEX* (Zamojski et al. 2007), u/u^* from MegaCam/CFHT (Sawicki et al. 2019), g, r, i, z, y from Subaru/Hyper Suprime-Cam (Aihara et al. 2019), Y, J, H, and K_s from VIRCAM/VISTA (McCracken et al. 2012), and MIR data from *Spitzer*/IRAC Channels 1, 2, 3, and 4 (Ashby et al. 2013, 2015, 2018; Steinhardt et al. 2014). The optical and infrared photometry is extracted using the SEXTRACTOR and IRACLEAN codes, respectively. Since we are specifically interested in dwarfs, which have smaller angular sizes, the high resolution of the IRAC MIR imaging (2 arcsec; Fazio et al. 2004) is an advantage.

In the u-band footprint, the catalogue offers photometry from two virtually identical filters, u and u^*. The u filter has a slightly shorter central wavelength and has replaced u^* in recent CFHT surveys, such as the Large Area U-band Deep Survey (CLAUDS; Sawicki et al. 2019). While the two filters span a similar wavelength range, the u filter does not cover the full COSMOS field. u^* data are deeper in the central region than the u band that, however, is more uniform across the field. For our work, we use the deeper of the two bands when both are available. The filterset available spans emission from starlight through to the hot dust that is likely to be associated with the AGN (e.g. Hickox & Alexander 2018). The IRAC wavebands are able to provide significant discrimination between the MIR emission

produced by stellar populations from that originating from the AGN (e.g. Assef et al. 2010).

2.2 Environmental parameters

Since we are interested in probing the role of environment in AGN triggering, we estimate environmental parameters using the DIScrete PERsistent Structure Extractor (DISPERSE; Sousbie, Pichon & Kawahara 2011). Following Laigle et al. (2018) and Lazar et al. (2023), we use DISPERSE to construct topological maps of the large-scale structure within the COSMOS footprint, in our redshift range of interest.[1]

DISPERSE computes a discrete Morse complex, using the Delaunay tessellation field estimator (DTFE; Schaap & van de Weygaert 2000; Cautun & van de Weygaert 2011) to create a density map. It first uses galaxy positions to compute Delaunay tessellations, i.e. the triangulation of discrete points such that no points from the defining distribution are within any of the resulting triangles. It then computes the density (δ) of the resulting cells, where δ = (area of cell)$^{-1}$, and identifies the locations of stationary points (i.e. maxima, minima, and saddle points). Finally, from this computed density field, segments are used to connect the nodes with the saddle points. The set of segments represents the filamentary structure of the cosmic web.

DISPERSE utilizes the concept of persistence to ensure the robustness of its density maps. It defines a persistence parameter (N) that serves as a threshold for the critical pairs that contribute to the density map and is important for constructing a robust filament structure devoid of noisy structures. The algorithm only retains critical pairs which have Poisson probabilities above $N\sigma$ from the mean. Following Laigle et al. (2018) and Lazar et al. (2023), we set N equal to 2. We use massive ($M_\star > 10^{10}$ M$_\odot$) galaxies to build our density maps, as they dominate the local gravitational potential, with the thicknesses of the slices ($\delta z \sim 0.03$) being driven by the median redshift uncertainties of the massive galaxies.

2.3 Sample selection

As noted in the introduction, given the depth of the photometry in COSMOS2020, complete samples of dwarfs can be constructed down to $M_\star \sim 10^8$ M$_\odot$, out to at least $z \sim 0.3$ (e.g. Jackson et al. 2021). For our study, we leverage the COSMOS2020 catalogue to pre-select our galaxies as follows. Tests indicate that, for the same set of UV–MIR photometric data points, the stellar masses outputted by PROSPECTOR are slightly larger than those produced by LEPHARE (which underpins COSMOS2020) by around 0.3 dex (this trend has also been noted by Pacifici et al. 2023). Our pre-selected sample consists of COSMOS2020 galaxies at $0.1 < z < 0.3$ in which the 16th percentile (i.e. the -1σ) value of the probability density function of the stellar mass is greater than $10^{7.5}$ M$_\odot$ and the 84th percentile (i.e. the $+1\sigma$) value is less than $10^{9.5}$ M$_\odot$.

There are ∼6500 such COSMOS2020 objects that are both classified as galaxies in this catalogue (`lp_type = 0`) and as 'extended' (i.e. galaxies) in the g, r, i, and z bands by the HSC pipeline and which lie outside masked regions such as bright star masks and image edges. Of these, 1146 galaxies have the full complement of UV to MIR photometry. These galaxies form the initial sample of objects on which we perform SED fitting using PROSPECTOR, as described in Section 3 below. For each galaxy, we use the photometric redshift from the COSMOS2020 catalogue and the median stellar mass as a first guess in the SED-fitting process. As described in Section 4 below, when identifying AGN and studying their properties, we refine the sample further, by applying additional cuts on redshift accuracy and the quality of the SED fits from PROSPECTOR.

2.4 Morphological classification using *HST F*814*W* images

We use visual inspection of *HST F*814*W* (*I*-band) images of the COSMOS field (Koekemoer et al. 2007; Massey et al. 2010) to morphologically classify our dwarf galaxy sample. These images have a 5σ point-source depth of 27.8 mag and an angular resolution of ∼0.05 arcsec. The visual inspection is performed by one expert classifier (SK). We classify our dwarfs into two broad morphological classes: early-type galaxies (ETGs) and late-type galaxies (LTGs). We also flag galaxies that show evidence of an ongoing or recent interaction e.g. tidal features, internal asymmetries or tidal bridges due to an ongoing merger with another galaxy. Fig. 1 presents example images of our dwarfs, including ETGs (top row), LTGs (middle row), and interacting systems (bottom row). Images in the first three columns in the bottom row show examples of interacting ETGs, while the last three columns show examples of interacting LTGs.

3 SED FITTING USING PROSPECTOR

We use PROSPECTOR, a PYTHON-based SED-fitting code to fit the photometry of our dwarf sample. PROSPECTOR is a Bayesian forward-modelling code (see table 1 in Pacifici et al. 2023, for a list of popular codes in the current literature) that can be used to infer galaxy properties, using either photometric or spectro-photometric data. PROSPECTOR is able to fit either parametric or non-parametric star formation histories (SFHs) to galaxy data and simultaneously constrain the AGN contribution to the SED. The code uses the Flexible Stellar Population Synthesis package (FSPS; Conroy, Gunn & White 2009) to generate SED models on the fly using PYTHON-FSPS (Foreman-Mackey, Sick & Johnson 2014).

We sample the posterior parameter distribution using DYNESTY (Speagle 2020), which utilizes the dynamic nested sampling algorithms of Higson et al. (2019). We adopt the non-parametric CONTINUITY-SFH models within PROSPECTOR as a basis for our analysis. Compared to their parametric counterparts, non-parametric models can typically explore more complex SFHs, which can include features like starbursts and episodes of quenching and rejuvenation (e.g. Simha et al. 2014; Diemer et al. 2017; Leja et al. 2019; Johnson et al. 2021), which are challenging to explore using parametric models (e.g. Suess et al. 2022).

The parameters in the PROSPECTOR model that we use for our analysis are briefly described below and summarized in Table 1.

(i) **SFH:** We implement CONTINUITY-SFH by adopting six age bins divided logarithmically, except the first two age bins which are fixed at 0–30 Myr, 30–100 Myr, and the final age bin which is fixed to cover 15 per cent of the age of the Universe. We utilize the Student's t-distribution for the prior (the log of the ratio of the SFRs in adjacent bins) with $\mu = 2$ (where μ is the number of degrees of freedom) and a scale-factor (σ) of 0.3.

(ii) **Stellar mass:** We adopt a uniform prior for the log of the stellar mass in the range $5 < \log(M_\star/\mathrm{M}_\odot) < 13$.

(iii) **Stellar metallicity:** A uniform prior is adopted for the log of the stellar metallicity in the range $-2.0 < \log(Z_\star/\mathrm{Z}_\odot) < 0.2$ following Leja et al. (2017). This range brackets the stellar

[1]Libeskind et al. (2018) provide a comprehensive comparison of filament finding algorithms, including DISPERSE.

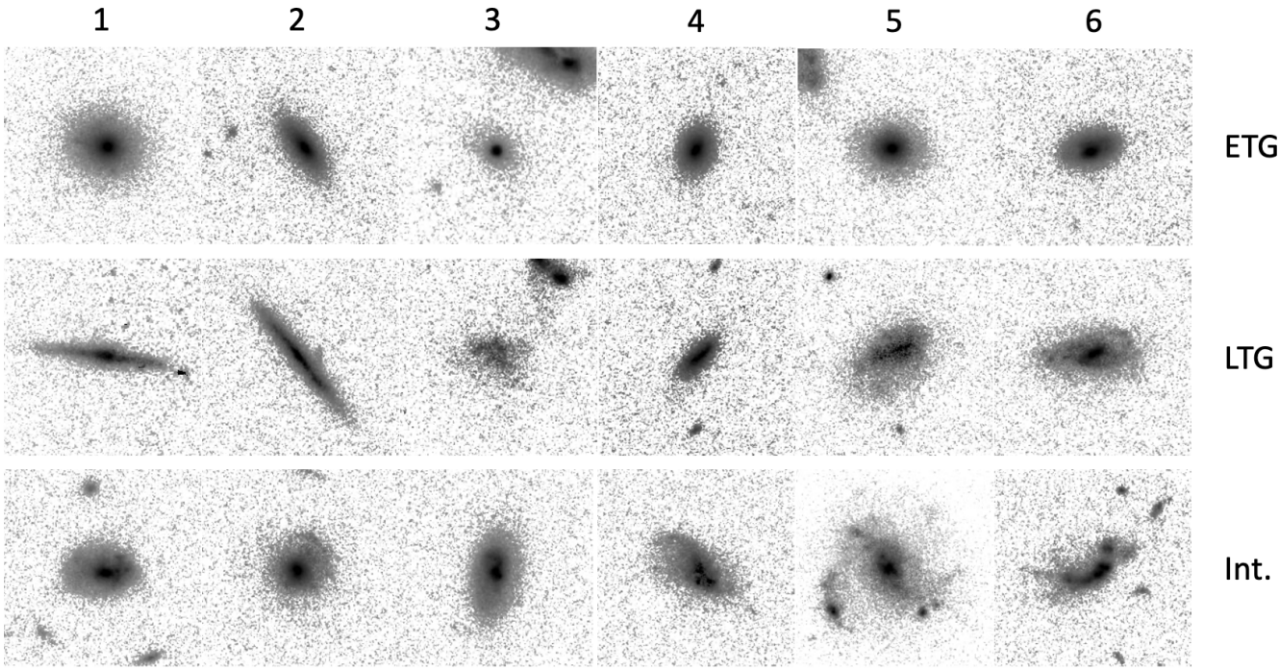

Figure 1. Example *HST F*814*W* images of dwarf galaxies in our sample, including ETGs (top row), LTGs (middle row), and interacting systems (bottom row). In the bottom row, the images in the first three columns show examples of interacting ETGs, while the last three columns show examples of interacting LTGs. Each image has a size of 5 arcsec on a side. At the median redshift of our dwarf sample ($z \sim 0.21$), this corresponds to a physical size of around 18 kpc.

Table 1. SED-fitting parameters, and their associated priors, in our PROSPECTOR model.

Parameter	Prior	Description
$\log(M_\star/\mathrm{M}_\odot)$	Uniform (min = 5, max = 13)	Stellar mass
$\log r_\mathrm{i}$	Student's *t*-distribution	Ratio of SFRs in adjacent bins
$\log(Z_\star/Z_\odot)$	Uniform (min = −2.0, max = 0.2)	Stellar metallicity
$\tau_{5500,\mathrm{diffuse}}$	Clipped normal (mean = 0.3, std. dev. = 1.0, min = 0, max = 4)	Optical depth of diffuse dust
$\tau_{\mathrm{young}}/\tau_{\mathrm{diffuse}}$	Clipped normal (mean = 1, std. dev. = 0.3, min = 0, max = 1.5)	Ratio of optical depth of birth clouds to optical depth of diffuse dust
Γ_{dust}	Clipped normal (mean = 0, std. dev. = 0.5, min = −1, max = 0.4)	Delta of the slope of attenuation curve compared to Calzetti law
U_{min}	Uniform (min = 0.1, max = 25)	Minimum intensity of light affecting the dust
Q_{PAH}	Uniform (min = 0.5, max = 7)	Fraction of dust mass in PAHs
$\log \gamma_{\mathrm{dust}}$	Uniform (min = −3, max = 0.15)	Fraction of dust mass exposed to U_{min}
$\log f_{\mathrm{AGN}}$	Uniform (min = −5, max = 3)	AGN luminosity as a fraction of the galaxy's bolometric luminosity
$\log \tau_{\mathrm{AGN}}$	Uniform (min = 5, max = 150)	Optical depth of the AGN torus
$\log U_{\mathrm{gas}}$	Uniform (min = −4, max = 1)	Gas phase ionization parameter

metallicities observed in nearby dwarf galaxies (e.g. Gallazzi et al. 2005; Panter et al. 2008).

(iv) **Dust attenuation:** Following Johnson et al. (2021), we implement the two-component Charlot & Fall (2000) dust model that treats the effect of dust from birth clouds (which impacts young stars) separately from that due to the diffuse dust (which impacts light from both young and old stars). Following Kriek & Conroy (2013), the strength of the UV bump is tied to the power-law index of the curve (because steeper attenuation laws tend to have stronger bumps). As described in Table 1, the three parameters used to describe dust attenuation are the optical depth of the diffuse dust ($\tau_{5500,\mathrm{diffuse}}$), the ratio of the optical depth of the birth clouds to that due to the diffuse dust ($\tau_{\mathrm{young}}/\tau_{\mathrm{diffuse}}$), and a delta modifier (Γ_{dust}) to the slope of the Calzetti dust law (Calzetti et al. 2000).

(v) **Dust emission:** The dust templates adopted (Draine & Li 2007) include infrared emission from small and large dust grains and polycyclic aromatic hydrocarbons (PAHs). The model includes three free parameters: U_{min}, γ_{dust}, and Q_{PAH}. γ_{dust} describes the fraction of dust mass affected by the minimum intensity of starlight required to heat up the diffuse dust and interstellar medium in the galaxy (U_{min}). Q_{PAH} describes the fraction of dust mass contributed by PAHs, which are responsible for strong emission in the MIR wavelengths. A uniform prior is adopted for all three free parameters within the ranges shown in Table 1.

(vi) **AGN templates:** The AGN templates adopted by PROSPECTOR are based on the CLUMPY models (Nenkova et al. 2008a,b) and include two free parameters: f_{AGN} and τ_{AGN}. f_{AGN} describes the ratio of the AGN luminosity to the galaxy's bolometric luminosity, while the latter describes the optical depth of the AGN torus. We adopt a uniform prior in the log of these parameters, within the ranges shown in Table 1.

(vii) **Nebular emission:** Nebular emission in PROSPECTOR uses the FSPS implementation of the CLOUDY photoionization code (Ferland et al. 2013), where the ionizing sources are the stellar populations produced by FSPS, as described by Byler et al. (2017). The model is parametrized by the gas phase metallicity and the ionization parameter, $U_{\rm gas}$ (Leja et al. 2017). Following the default implementation within PROSPECTOR, we tie the gas-phase metallicity to the stellar metallicity and allow the log of the ionization parameter to vary between −4 and 1.

We consider the acceptability of our fits following Smith et al. (2012). A fit is considered to be acceptable if its best-fitting χ^2 is below the 99 per cent confidence threshold for the given number of photometric bands. We fit each galaxy with and without the AGN templates. We use the ratio of the χ^2 of the best-fitting model with and without the AGN templates to estimate the significance of including an AGN in the fit. As described in Section 4.1 below, we then use that information, together with the value of $f_{\rm AGN}$, to identify dwarfs that are likely to show signs of AGN activity.

4 AGN IN NEARBY DWARF GALAXIES

In this section, we use the outputs from our SED fitting to probe the incidence of AGN in nearby dwarfs, study the role of interactions and environment in AGN triggering, and compare the star formation activity in dwarf AGN to their non-AGN counterparts. For the analysis below, we restrict our initial sample of 1146 galaxies to those that have photometric redshift errors less than 20 per cent and have acceptable fits as described above. This produces a final sample of 508 dwarf galaxies that underpins our analysis below. Of these, 476 galaxies (i.e. around 94 per cent) lie within the *HST* footprint and our morphological analysis in Section 4.3 is therefore restricted to these systems. It is worth noting that, by construction, the AGN that we study here are only those that are radiatively efficient and leave a signature in the UV to MIR wavelengths. The stellar mass and SFR values used in our analysis below are the median values of these parameters, calculated using PROSPECTOR, for each galaxy.

4.1 The incidence of AGN in dwarf galaxies

While we use the median values of stellar mass and SFR, we employ the fifth percentile values of $f_{\rm AGN}$, denoted by $f_{\rm AGN,5}$ hereafter, to identify dwarfs which show signs of AGN activity in our sample. This ensures that 95 per cent of the $f_{\rm AGN}$ distribution in each galaxy is above the chosen threshold that defines an AGN. This is more conservative than using, for example, the 16th percentile value, as in other recent studies (e.g. Best et al. 2023; Das et al. 2024). Fig. 2 presents the values of $f_{\rm AGN,5}$ in our final sample of dwarfs. The bimodality of the distribution (around $\log f_{\rm AGN,5} \sim -2.8$) suggests the presence of a population of AGN in these dwarf galaxies that could be demarcated by this value. We use this distribution to define AGN as galaxies where (1) $\log f_{\rm AGN,5} > -2.8$ and (2) including the AGN in the fitting improves the quality of the fit (i.e. the χ^2 value of the best-fitting model with AGN templates included is smaller than its counterpart without an AGN). The red histogram denotes the galaxy population that we define to be AGN in our sample. The grey histogram denotes non-AGN i.e. galaxies that either have $\log f_{\rm AGN,5} < -2.8$ or have $\log f_{\rm AGN,5} > -2.8$ but where including the AGN templates does not result in a better fit.

It is worth noting that the typical spatial scales of accretion discs are around $\sim 10^{-2}$ pc (e.g. Hawkins 2007). This is around 5 orders of magnitude smaller on a linear scale (and therefore around 15 orders of magnitude smaller in terms of volume) than the host dwarf galaxies, which have spatial scales of around a kpc (e.g. Watkins et al. 2023). Values of $\log f_{\rm AGN,5}$ values greater than −2.8 (i.e. $f_{\rm AGN,5}$ values greater than ∼0.16 per cent) may therefore represent relatively bright radiatively efficient AGN in our dwarf population. Given the selection criteria above, around a third (162 out of 508 or 32 ± 2 per cent) of the dwarfs in our sample show signs of AGN activity.

In Fig. 3, we show the contribution of dwarf AGN in different parts of the $f_{\rm AGN,5}$ versus stellar mass space to the overall percentage of galaxies classified as AGN in our dwarf sample. The histogram

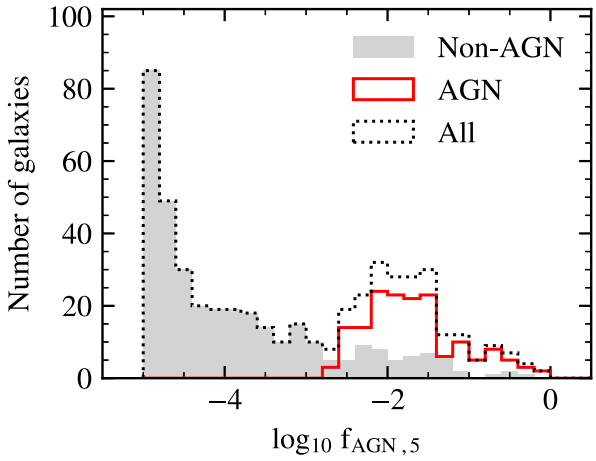

Figure 2. Distribution of $f_{\rm AGN,5}$ in our final sample of 508 dwarf galaxies, which exhibits a bimodality around $\log f_{\rm AGN,5} \sim -2.8$. The red histogram denotes galaxies that we define to be AGN. These are galaxies that have $\log f_{\rm AGN,5} > -2.8$ and in which including the AGN in the fitting improves the quality of the fit (i.e. the χ^2 value of the best-fitting model with an AGN template included is smaller than its counterpart without an AGN). The grey histogram corresponds to galaxies that are classified as non-AGN. These are systems that either have $\log f_{\rm AGN,5} < -2.8$ or where $\log f_{\rm AGN,5} > -2.8$ but including the AGN does not result in a better fit (see the text in Section 4.1 for more details).

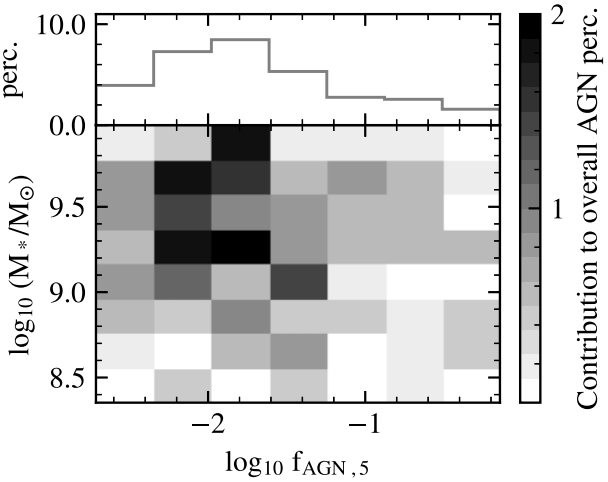

Figure 3. The contribution of dwarf AGN in different parts of the PROSPECTOR-derived stellar mass versus $f_{\rm AGN,5}$ parameter space to the overall AGN percentage in our dwarf sample. The histogram shows how this contribution varies as a function of $f_{\rm AGN,5}$ (regardless of the value of stellar mass). Summing the numbers in either the heatmap or the histogram yields the overall AGN percentage of ∼32 per cent.

shows how this contribution varies as a function of $f_{\rm AGN,5}$ (regardless of the value of stellar mass). Summing the numbers in the heatmap or the histogram yields the overall AGN percentage (around 32 per cent) within our dwarf sample. Recall that the galaxy population studied here is likely to be complete down to $M_\star \sim 10^8$ M$_\odot$, out to $z \sim 0.3$ (Jackson et al. 2021).

While past studies have estimated BH occupation and active fractions in dwarfs via different methods, our estimate for the AGN fraction in dwarfs is consistent with the findings of the recent dwarf literature. Recent work indicates that the BH occupation fraction in dwarfs is likely to be high (estimates typically vary between 40 and 100 per cent within the stellar mass range probed in this study, see e.g. Ricarte & Natarajan 2018; Bellovary et al. 2019; Nguyen et al. 2019). Inevitably, the active fractions are lower.

For example, Mezcua & Domínguez Sánchez (2024) use spatially resolved emission-line diagnostics from integral-field spectroscopy to estimate an AGN fraction of 20 per cent in SDSS dwarfs. This is consistent with the fractions found using MIR photometry (10–30 per cent; e.g. Kaviraj et al. 2019). It is interesting to note that the AGN fractions derived using a spaxel-by-spaxel analysis, as performed by Mezcua & Domínguez Sánchez (2024), are much larger than those derived using single fibre diagnostics in the SDSS (∼1 per cent). This is because, as noted in the introduction, the star formation activity across the galaxy is likely to swamp the emission-line signal due to the AGN in the highly star-forming dwarfs that are detectable in the SDSS. A spatially resolved analysis, on the other hand, is able to isolate the region that may host an AGN, thus enabling a more sensitive probe of its existence within the galaxy. Interestingly, Dickey et al. (2019) use a sample of dwarfs with a median redshift of $z \sim 0.024$ to show that, in the very nearby Universe – where relatively unbiased dwarf samples can be constructed even using the SDSS – around ∼80 per cent of quiescent dwarf galaxies in low-density environments show central AGN-like emission-line ratios.

Pacucci, Mezcua & Regan (2021) estimate that 5–22 per cent of the BHs in the dwarf population are likely to be active. This rises to around 30 per cent if the host metallicities are lower ($Z < Z_\odot$), which is indeed the case for dwarf galaxies (e.g. Gallazzi et al. 2005; Panter et al. 2008). Davis et al. (2022) combine deep radio and optical data, from LOFAR and HSC, respectively, with theoretical models to conclude that AGN triggering in dwarfs is likely to be stochastic and a common phenomenon. This appears consistent with the observation that dwarfs may lie on an extrapolation of the M–σ relation seen in massive galaxies (e.g. Schutte, Reines & Greene 2019; Davis et al. 2020). Since BH feedback predicts a universal M $\propto \sigma^4$ relation (e.g. Silk & Rees 1998; King & Nealon 2021), this suggests that frequent AGN activity could be important in the dwarf regime, consistent with the incidence of AGN being derived by recent work, including this study. Taken together, these studies suggest a growing consensus that a significant minority of dwarfs in the nearby Universe show signs of AGN activity.

4.2 The role of environment in triggering dwarf AGN

We proceed by comparing the environments of our dwarf AGN to their non-AGN counterparts. For this analysis, we consider galaxies in the redshift range $0.2 < z < 0.3$ because the relatively small number of massive galaxies at $z < 0.2$ means that reliable density maps cannot be created for these redshifts. To perform this comparison, we construct a control sample of dwarfs in which $\log f_{\rm AGN,5} < -2.8$ and which has the same distributions of stellar mass and redshift as their dwarf AGN counterparts.[2]

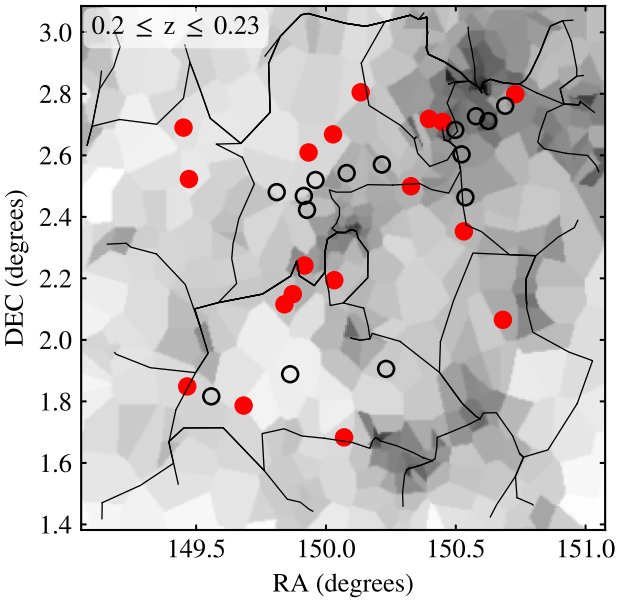

Figure 4. An example density map, generated using DISPERSE, as described in Section 2.2. The redshift limits of the map are shown in the top left-hand corner. Filaments are shown using solid lines, with a random subset of AGN (filled red circles) and non-AGN (open black circles) shown overplotted.

In Fig. 4, we show an example density map, created using DISPERSE as described in Section 2.2. The filaments are shown using solid lines and random examples of dwarf AGN and control galaxies that reside within the redshift slice are indicated using filled red and open black circles respectively. In Fig. 5, we present the distributions of the projected distances to the nearest filaments, nodes, and massive galaxies for the AGN and the control sample. Median values and their associated uncertainties, calculated via bootstrapping, are shown using the vertical lines and also described in rows 1, 2, and 3 of Table 2.

Applying a two-sample Kolmogorov–Smirnov (KS) test to the AGN and control distributions produces p-values of 0.25, 0.45, and 0.99 for the distances to nodes, filaments, and massive galaxies, respectively. Based on both the median values and their uncertainties and the results of the KS tests, we do not find evidence of a difference in these distances between the AGN and their control counterparts. This suggests that the environment in which they reside is unlikely to play a significant role in AGN triggering.

While various studies have probed the role of environment using different methods, our conclusions appear consistent with the results of other recent work that has explored the dwarf regime. For example, Kristensen, Pimbblet & Penny (2020), who define local environment using the distance to the tenth nearest neighbour, find that environment is not an important factor in triggering AGN activity in dwarfs. This is similar to the results of Sabater, Best & Heckman (2015), whose galaxy sample includes objects at the upper mass end

[2]We construct the control sample as follows. For each AGN, we identify all non-AGN with $\log f_{\rm AGN,5} < -2.8$ within stellar mass and redshift tolerances of 0.05 dex and 0.04, respectively. We then select, at random, one of these galaxies to be the control counterpart of the AGN in question. No control galaxy is assigned to more than one AGN. The results in this section do not change if different tolerances are used.

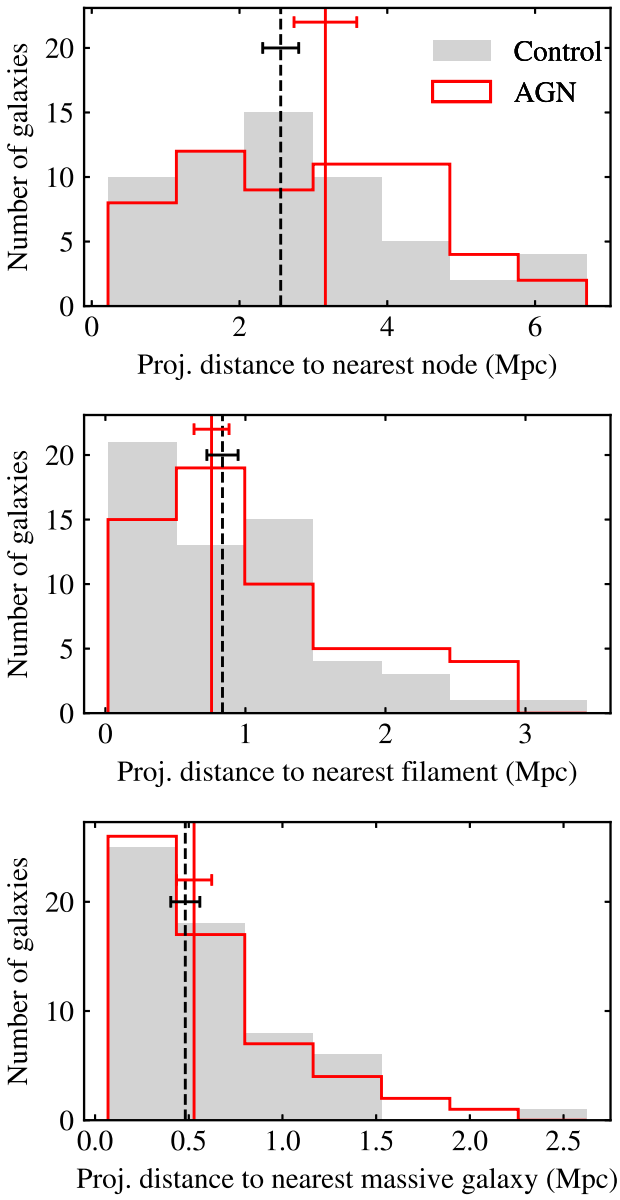

Figure 5. Projected distances to nearest nodes (top), filaments (middle), and massive galaxies (bottom) for dwarf AGN (red) and the control sample of non-AGN (grey).

of the dwarf regime. They find that the effect of either the local density or galaxy interactions is minor in the prevalence of AGN activity.

4.3 Morphology and the role of interactions in AGN triggering

In this section, we consider the morphological properties of our dwarf AGN compared to their non-AGN counterparts. Recall from Section 4.3 that morphological information is available for 476 galaxies out of the final sample of 508 that lie within the *HST* footprint. In a similar vein to Section 4.3, we construct a control sample that is matched in stellar mass and redshift to the AGN (but this time without any restriction in redshift).

In rows 4 and 5 of Table 2, we summarize the fraction of AGN and control galaxies that are classified as ETGs and interacting, respectively. The ETG and interacting fractions in the AGN and control samples are indistinguishable, given the uncertainties. The similar interacting fractions, combined with the fact that interactions reinforce dispersion-dominated ETG-like structures over time (e.g. Martin et al. 2018), suggest that this process does not play a significant role in triggering the AGN in this study. This result appears aligned with the findings of Kaviraj et al. (2019), who have shown that the fraction of dwarf AGN in ongoing mergers does not appear to show an excess compared to that in their control counterparts. It is also consistent with the fact that AGN appear not to preferentially occupy regions of higher density (from Section 4.2) where the incidence of interactions is likely to be higher. Finally, it is worth noting that the lack of influence of either local environment or the presence of interactions appears consistent with the conclusions of Davis et al. (2022) that AGN triggering in the dwarf regime may be a largely stochastic process.

4.4 Star formation activity in dwarf AGN

We conclude our study by exploring whether there are differences in the star formation activity of dwarfs that contain AGN and those that do not. In particular, it is interesting to explore whether, given their relatively shallow potential wells, dwarf galaxies may be more susceptible to prompt quenching of star formation than their massive counterparts. In row 6 of Table 2, we compare the median values of the sSFRs, and their associated uncertainties, in dwarf AGN with those of the control sample defined in Section 4.3. Given the median values and their uncertainties, the star formation activity in the AGN is marginally lower compared to those in their control counterparts. However, we do not find evidence of a significant, prompt quenching of star formation in dwarf galaxies that host AGN activity.

It is worth discussing this result in the context of AGN feedback suppressing star formation in dwarf galaxies, the potential for which has been demonstrated from both theoretical (Barai & de Gouveia Dal Pino 2019; Koudmani, Sijacki & Smith 2022; Arjona-Galvez, Di Cintio & Grand 2024) and empirical (e.g. Penny et al. 2018) points of view. Recent work has shown that the presence of AGN feedback does not necessarily manifest itself in lower instantaneous SFRs during individual star formation episodes (e.g. Ward et al. 2022). Rather, the indicators of quenching correlate more strongly with the BH mass, which is a measure of the cumulative output of the AGN over the lifetime of the galaxy (e.g. Piotrowska et al. 2022). While measuring BH masses is beyond the scope of this study, we note that our results do not argue against AGN feedback having an influence on star formation in the dwarf regime. Indeed, recent work (e.g. Davis et al. 2022) has suggested that the central gas reservoirs in dwarfs are much larger than what is required to fuel the BH and the energetics suggest that AGN feedback is both plausible and likely in these systems.

5 SUMMARY

We have employed SED fitting via PROSPECTOR using deep UV to MIR broad-band photometry in the COSMOS field, to search for radiatively efficient AGN in nearby ($0.1 < z < 0.3$) dwarf (10^8 $M_\odot < M_\star < 10^{10}$ $M_\odot$) galaxies. We have explored the percentage of nearby dwarfs that show signs of AGN activity, investigated the potential role of environment and interactions in triggering our AGN, and studied whether the sSFRs of our AGN are different from their non-AGN counterparts. Our main conclusions are as follows:

(i) Around a third (32 ± 2 per cent) of dwarf galaxies in our sample show signs of AGN activity, consistent with the dwarf AGN fractions derived, via various techniques, in the recent literature.

Table 2. Comparisons of various quantities between dwarf AGN and control samples constructed from the non-AGN dwarfs that have the same distributions of redshift and stellar mass as the AGN. Note that, while the analysis in rows 1–3 is restricted to the redshift range $0.2 < z < 0.3$ (because, as noted in Section 4.2, there are not enough massive galaxies to create reliable density maps at $z < 0.2$), the analysis in rows 4–6 uses the full redshift range of our study ($0.1 < z < 0.3$). Rows 1–3 compare the distances to nodes, filaments and massive galaxies of the AGN and their control counterparts. The number of AGN on which this environmental analysis is based is 63. Rows 4 and 5 compare the fractions of AGN and control galaxies that are classified as ETGs and interacting, respectively. The number of AGN that have *HST* images and underpin the analysis in these rows is 155. The uncertainties in rows 1–5 are calculated following Cameron (2011). Row 6 compares the median specific SFR (sSFR) of dwarf AGN to their control counterparts. The number of AGN that underpins this analysis is 162. The uncertainties in this row are calculated via bootstrapping.

	AGN	Control
Median projected distance to nearest node (Mpc)	3.16 ± 0.42	2.56 ± 0.24
Median projected distance to nearest filament (Mpc)	0.76 ± 0.13	0.84 ± 0.11
Median projected distance to nearest massive galaxy (Mpc)	0.53 ± 0.09	0.48 ± 0.08
Fraction of galaxies which are ETGs	0.30 ± 0.04	0.33 ± 0.04
Fraction of galaxies that are interacting	0.14 ± 0.03	0.16 ± 0.03
Median log (sSFR/yr^{-1})	− 10.37 ± 0.05	− 10.22 ± 0.04

(ii) The local environments of dwarf AGN, parametrized by the projected distances to nodes, filaments, and massive galaxies, are indistinguishable from those of a control sample (which has the same distribution of redshift and stellar mass) constructed from non-AGN dwarfs. This suggests that local environment is not likely to play a significant role in AGN triggering.

(iii) The early-type and interacting fractions in our AGN are also indistinguishable from those of a control sample, suggesting that the onset of AGN, at least in the sample studied here, is not strongly influenced by galaxy interactions.

(iv) Given the median values of sSFR and their uncertainties, the star formation activity in dwarf AGN is marginally lower compared to those in their control counterparts. However, we do not find strong evidence of a significant, prompt quenching of star formation in dwarf galaxies that host AGN activity.

Our study adds to the burgeoning body of work that suggests that a significant minority of nearby dwarf galaxies show signs of AGN activity. It also demonstrates the potential of SED fitting for exploring AGN populations within dwarfs in future multiwavelength deep-wide data sets. These studies will be important, both for putting such results on a firmer statistical footing and for exploring how the AGN populations in dwarfs may evolve over cosmic time.

ACKNOWLEDGEMENTS

We thank the referee for several constructive comments that improved the presentation of the paper. BB and IL acknowledge PhD studentships from the Centre for Astrophysics Research at the University of Hertfordshire. SK and AEW acknowledge support from the STFC (grant numbers ST/S00615X/1 and ST/X001318/1). SK also acknowledges a Senior Research Fellowship from Worcester College Oxford. SD acknowledges support from the STFC via grant ST/W507490/1. DJBS acknowledges support from the STFC via grant ST/V000624/1. For the purpose of open access, the author has applied a Creative Commons Attribution (CC BY) licence to any Author Accepted Manuscript version arising from this submission.

DATA AVAILABILITY

The parameters calculated in this study can be shared upon reasonable request to the authors.

REFERENCES

Aihara H. et al., 2018, PASJ, 70, S8
Aihara H. et al., 2019, PASJ, 71, 114
Alam S. et al., 2015, ApJS, 219, 12
Arjona-Galvez E., Di Cintio A., Grand R. J. J., 2024, preprint (arXiv:2402.00929)
Ashby M. L. N. et al., 2013, ApJ, 769, 80
Ashby M. L. N. et al., 2015, ApJS, 218, 33
Ashby M. L. N. et al., 2018, ApJS, 237, 39
Assef R. J. et al., 2010, ApJ, 713, 970
Baldassare V. F., Geha M., Greene J., 2020, ApJ, 896, 10
Baldwin J. A., Phillips M. M., Terlevich R., 1981, PASP, 93, 5
Barai P., de Gouveia Dal Pino E. M., 2019, MNRAS, 487, 5549
Beckmann R. S. et al., 2017, MNRAS, 472, 949
Bellovary J. M., Cleary C. E., Munshi F., Tremmel M., Christensen C. R., Brooks A., Quinn T. R., 2019, MNRAS, 482, 2913
Best P. N. et al., 2023, MNRAS, 523, 1729
Byler N., Dalcanton J. J., Conroy C., Johnson B. D., 2017, ApJ, 840, 44
Calzetti D., Armus L., Bohlin R. C., Kinney A. L., Koornneef J., Storchi-Bergmann T., 2000, ApJ, 533, 682
Cameron E., 2011, PASA, 28, 128
Cautun M. C., van de Weygaert R., 2011, preprint (arXiv:1105.0370)
Charlot S., Fall S. M., 2000, ApJ, 539, 718
Cid Fernandes R., Stasińska G., Schlickmann M. S., Mateus A., Vale Asari N., Schoenell W., Sodré L., 2010, MNRAS, 403, 1036
Cid Fernandes R., Stasińska G., Mateus A., Vale Asari N., 2011, MNRAS, 413, 1687
Conroy C., Gunn J. E., White M., 2009, ApJ, 699, 486
Das S. et al., 2024, MNRAS, 531, 977
Davies R. L. et al., 2024, MNRAS, 528, 4976
Davis T. A. et al., 2020, MNRAS, 496, 4061
Davis F. et al., 2022, MNRAS, 511, 4109
Delvecchio I. et al., 2014, MNRAS, 439, 2736
Delvecchio I. et al., 2017, A&A, 602, A3
Dickey C. M., Geha M., Wetzel A., El-Badry K., 2019, ApJ, 884, 180
Diemer B., Sparre M., Abramson L. E., Torrey P., 2017, ApJ, 839, 26
Draine B. T., Li A., 2007, ApJ, 657, 810
Driver S. P. et al., 2022, MNRAS, 513, 439
Dubois Y. et al., 2021, A&A, 651, A109
Fabian A. C., 2012, ARA&A, 50, 455
Fazio G. G. et al., 2004, ApJS, 154, 10
Ferland G. J. et al., 2013, Rev. Mex. Astron. Astrofis., 49, 137
Foreman-Mackey D., Sick J., Johnson B., 2014, python-fsps: Python bindings to FSPS (v0.1.1), https://doi.org/10.5281/zenodo.12157
Gaia Collaboration et al., 2016, A&A, 595, A1
Gallazzi A., Charlot S., Brinchmann J., White S. D. M., Tremonti C. A., 2005, MNRAS, 362, 41

Greene J. E., Ho L. C., 2007, ApJ, 670, 92
Gürkan G. et al., 2018, MNRAS, 475, 3010
Hawkins M. R. S., 2007, A&A, 462, 581
Hickox R. C., Alexander D. M., 2018, ARA&A, 56, 625
Higson E., Handley W., Hobson M., Lasenby A., 2019, Stat. Comput., 29, 891
Ivezić Ž. et al., 2019, ApJ, 873, 111
Jackson R. A. et al., 2021, MNRAS, 502, 4262
Johnson B. D., Leja J. L., Conroy C., Speagle J. S., 2019, Astrophysics Source Code Library, record ascl:1905.025
Johnson B. D., Leja J., Conroy C., Speagle J. S., 2021, ApJS, 254, 22
Kaviraj S. et al., 2017, MNRAS, 467, 4739
Kaviraj S., Martin G., Silk J., 2019, MNRAS, 489, L12
Kewley L. J., Dopita M. A., Sutherland R. S., Heisler C. A., Trevena J., 2001, ApJ, 556, 121
King A., Nealon R., 2021, MNRAS, 502, L1
Koekemoer A. M. et al., 2007, ApJS, 172, 196
Koudmani S., Sijacki D., Smith M. C., 2022, MNRAS, 516, 2112
Kriek M., Conroy C., 2013, ApJ, 775, L16
Kristensen M. T., Pimbblet K., Penny S., 2020, MNRAS, 496, 2577
Laigle C. et al., 2016, ApJS, 224, 24
Laigle C. et al., 2018, MNRAS, 474, 5437
Latimer L. J., Reines A. E., Plotkin R. M., Russell T. D., Condon J. J., 2019, ApJ, 884, 78
Lazar I., Kaviraj S., Martin G., Laigle C., Watkins A., Jackson R. A., 2023, MNRAS, 520, 2109
Lazar I., Kaviraj S., Watkins A. E., Martin G., Bichang'a B., Jackson R. A., 2024, MNRAS, 529, 499
Leja J., Johnson B. D., Conroy C., van Dokkum P. G., Byler N., 2017, ApJ, 837, 170
Leja J., Johnson B. D., Conroy C., van Dokkum P., 2018, ApJ, 854, 62
Leja J., Carnall A. C., Johnson B. D., Conroy C., Speagle J. S., 2019, ApJ, 876, 3
Libeskind N. I. et al., 2018, MNRAS, 473, 1195
Lofthouse E. K., Kaviraj S., Smith D. J. B., Hardcastle M. J., 2018, MNRAS, 479, 807
Marleau F. R., Clancy D., Habas R., Bianconi M., 2017, A&A, 602, A28
Martin G., Kaviraj S., Devriendt J. E. G., Dubois Y., Pichon C., 2018, MNRAS, 480, 2266
Martin G. et al., 2019, MNRAS, 485, 796
Martínez-Palomera J., Lira P., Bhalla-Ladd I., Förster F., Plotkin R. M., 2020, ApJ, 889, 113
Massey R., Stoughton C., Leauthaud A., Rhodes J., Koekemoer A., Ellis R., Shaghoulian E., 2010, MNRAS, 401, 371
Mateo M. L., 1998, ARA&A, 36, 435
McCracken H. J. et al., 2012, A&A, 544, A156
Mezcua M., Domínguez Sánchez H., 2024, MNRAS, 528, 5252
Mezcua M., Civano F., Marchesi S., Suh H., Fabbiano G., Volonteri M., 2018, MNRAS, 478, 2576
Mezcua M., Suh H., Civano F., 2019, MNRAS, 488, 685
Nenkova M., Sirocky M. M., Ivezić Ž., Elitzur M., 2008a, ApJ, 685, 147
Nenkova M., Sirocky M. M., Nikutta R., Ivezić Ž., Elitzur M., 2008b, ApJ, 685, 160
Nguyen D. D. et al., 2019, ApJ, 872, 104
Nyland K. et al., 2017, ApJ, 845, 50
Pacifici C. et al., 2023, ApJ, 944, 141
Pacucci F., Mezcua M., Regan J. A., 2021, ApJ, 920, 134
Panter B., Jimenez R., Heavens A. F., Charlot S., 2008, MNRAS, 391, 1117
Penny S. J. et al., 2018, MNRAS, 476, 979
Piotrowska J. M., Bluck A. F. L., Maiolino R., Peng Y., 2022, MNRAS, 512, 1052
Reines A. E., Greene J. E., Geha M., 2013, ApJ, 775, 116
Reines A. E., Condon J. J., Darling J., Greene J. E., 2020, ApJ, 888, 36
Ricarte A., Natarajan P., 2018, MNRAS, 474, 1995
Richstone D. et al., 1998, Nature, 385, A14
Sabater J., Best P. N., Heckman T. M., 2015, MNRAS, 447, 110
Satyapal S., Abel N. P., Secrest N. J., 2018, ApJ, 858, 38
Sawicki M. et al., 2019, MNRAS, 489, 5202
Schaap W. E., van de Weygaert R., 2000, A&A, 363, L29
Schutte Z., Reines A. E., Greene J. E., 2019, ApJ, 887, 245
Shimwell T. W. et al., 2019, A&A, 622, A1
Silk J., 2017, ApJ, 839, L13
Silk J., Rees M. J., 1998, A&A, 331, L1
Simha V., Weinberg D. H., Conroy C., Dave R., Fardal M., Katz N., Oppenheimer B. D., 2014, preprint (arXiv:1404.0402)
Smith D. J. B. et al., 2012, MNRAS, 427, 703
Sousbie T., Pichon C., Kawahara H., 2011, MNRAS, 414, 384
Speagle J. S., 2020, MNRAS, 493, 3132
Steinhardt C. L. et al., 2014, ApJ, 791, L25
Strauss M. A. et al., 2002, AJ, 124, 1810
Suess K. A. et al., 2022, ApJ, 935, 146
Thorne J. E. et al., 2022, MNRAS, 509, 4940
Tolstoy E., Hill V., Tosi M., 2009, ARA&A, 47, 371
Volonteri M., Habouzit M., Colpi M., 2021, Nat. Rev. Phys., 3, 732
Ward S. R., Harrison C. M., Costa T., Mainieri V., 2022, MNRAS, 514, 2936
Watkins A. E., Salo H., Kaviraj S., Collins C. A., Knapen J. H., Venhola A., Román J., 2023, MNRAS, 521, 2012
Weaver J. R. et al., 2022, ApJS, 258, 11
Wright A. H. et al., 2017, MNRAS, 470, 283
York D. G. et al., 2000, AJ, 120, 1579
Zamojski M. A. et al., 2007, ApJS, 172, 468

This paper has been typeset from a TEX/LATEX file prepared by the author.